Sanchez, J, Stevens, MB, Young, AR, Gallo, A, Zhao, M, Liu, Y, Ramos-Garcés, MV, Ben-Naim, M, Colón, JL, Sinclair, R, King, LA, Bajdich, M and Jaramillo, TF (2021) Isolating the Electrocatalytic Activity of a Confined NiFe Motif within Zirconium Phosphate. Advanced Energy Materials, 11 (20). p. 2003545. ISSN 1614-6832

DOI: https://doi.org/10.1002/aenm.202003545

Publisher: Wiley

Version: Accepted Version

An Active Oxygen Evolution Electrocatalyst Motif Created by Confining Transition Metal Cations within Layered Structures

Joel Sanchez,[1,2,3] Michaela Burke Stevens,[1,2,3] Alexandra R. Young,[1] Alessandro A. Gallo,[2,3] Meng Zhao,[3] Mario V. Ramos-Garcés,[4] Jorge L. Colón,[4] Laurie A. King,[5] Michal Bajdich,[3] and Thomas F. Jaramillo[1,2,3]

[1]Department of Chemical Engineering, Stanford University, Stanford, CA 94035, USA
[2]SUNCAT Center for Interface Science and Catalysis, Stanford University, Stanford, CA 94035, USA
[3]SUNCAT Center for Interface Science and Catalysis, SLAC National Accelerator Laboratory, 2575 Sand Hill Road, Menlo Park, CA 94025, USA
[4]Department of Chemistry, University of Puerto Rico at Río Piedras, San Juan, PR 00925, USA
[5]Faculty of Science and Engineering, Manchester Metropolitan University, Manchester, M1 5GD, UK

KEYWORDS: zirconium phosphate, intercalation, confinement, nanoenvironment, oxygen evolution reaction, layered material, nonprecious metal, water electrocatalyst, metal-oxides, nickel, and iron.

Corresponding Authors: Laurie A. King (l.king@mmu.ac.uk), theory corresponding author Michal Bajdich (bajdich@slac.stanford.edu), and Thomas F. Jaramillo (jaramillo@stanford.edu)

Abstract

Unique classes of active-site motifs are needed to redefine and improve electrocatalysis. Herein we have engineered a new catalyst motif for the oxygen evolution reaction (OER) consisting of nickel-iron transition metal cations confined within a layered zirconium phosphate matrix. We find that with optimal intercalation, confined Ni/Fe catalysts have an order of magnitude improved mass activity compared to more conventional surface-adsorbed systems in 0.1 M KOH. Interestingly, the confined environments within the layered structure also stabilizes Fe-rich compositions (90%) that are difficult to study in more traditional formats. By grafting inert molecules to the outer surface we have evidence that the intercalated Ni/Fe cations stay within the interlayer during catalysis and serve as the active site. After determining a possible structure (wycherproofite), density theory was shown to correlate with the observed experimental compositional trends. We further identify that the improved activity of this motif is correlated to the Fe and water content/composition within the confined space. This work highlights the catalytic enhancement possibilities available through confined active-site motifs, thus opening new avenues to develop classes of improved catalysts within unique nanoscale chemical environments.

TOC Image

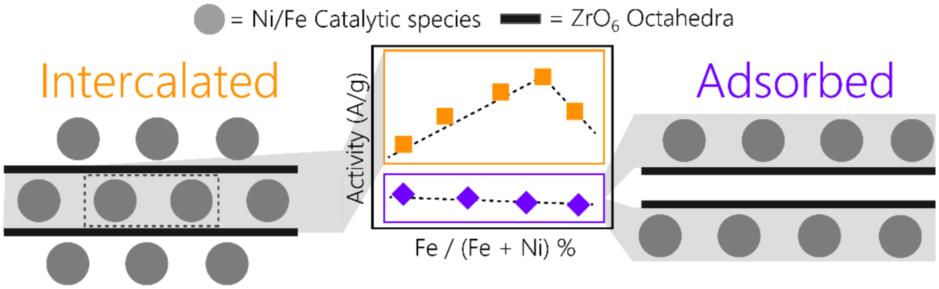

Introduction

The oxygen evolution reaction (OER) plays a key role in many emerging energy conversion technologies including but not limited to water electrolysis,[1] metal-air batteries,[2] and CO_2 electorlysis.[3] The use of alkaline electrolytes enables the use of non-precious metal catalysts such as *3d*-transition metal oxides[4,5], (oxy)-hydroxides[5], layered double hydroxides[6], metal organic frameworks (MOF)[7], and single-atom systems[8]. In particular, the doping of Fe into inactive Ni (oxy)hydroxide ($Ni(OH)_2$/NiOOH) materials has yielded high performing catalysts with long term durability.[5,9–14] Various promising routes have focused on increasing activity of these catalyst systems by methods that increase the number of active sites or increase the intrinsic activity of each site. While the former has been employed extensively in the literature, the latter has been difficult to ascertain. Herein, we create a new catalyst motif, breaking away from conventional surface based OER catalysts in the hopes of overcoming the bottlenecks that have hindered conventional catalyst systems for decades. This new motif involves confining Ni and Fe catalysts species within the θ phase of zirconium phosphate ($Zr(HPO_4)_2 \cdot 6H_2O$, a highly hydrated derivative of the more widely used $Zr(HPO_4)_2 \cdot H_2O$, α-zirconium phosphate).

Strategies such as the encapsulation or confinement of active species within layered materials have recently emerged in computational and experimental work as promising routes to enhanced activity.[15] Such strategies confine the active sites, influencing the reaction intermediates by providing microenvironments or solvation structures that have a significant effect on catalytic performance.[16–22] The act of catalyst confinement can potentially create unique active site environments that are not accessible by traditional surface-based motifs. Density functional theory (DFT) calculations have highlighted layered materials as a promising platform for breaking OER scaling relationships by providing a planar channel that has a unique microenvironment that enables new types of adsorbate-catalyst interactions.[23,24] Experimental work has shown that the confinement of active species within birnessite,[25–28] MoS_2,[29,30] and graphene[16,31,32] improve the activity, stability, and selectivity, respectively, of electrochemical reactions. With the increasing number of confined catalytic platforms, it is possible to build a template to provide experimental evidence showcasing the nature of active species within a confined space. Furthermore, in exploring confined environments, several effects are of interest that alter the chemical nature of the confined platform, including but not limited to interlayer spacing, interlayer solvation dynamics, and co-intercalated species. Understanding how these factors govern performance and elucidating if confined catalytic species are active motivates further study.

Of the numerous layered materials of interest for exploring confined environments, θ-zirconium phosphate ($Zr(HPO_4)_2 \cdot 6H_2O$) is one promising candidate that has shown impressive property and application tunability as a function of ion intercalation for a wide range of technologies including biosensors, [33–35] vapochromic materials,[36–38] and drug delivery.[39–43] However, for electrocatalysis, while layered and nanostructured (sheets, cubes, rods, and spheres) zirconium phosphate morphologies have shown promise as transition metal oxide supports, no intrinsic performance enhancements from confinement have previously been observed.[44–47] Extracting the factors that govern the enhancements in the nanoscopic channels could help the development of strategies and further the advancement of confined catalyst systems. [44–47]

In this work, zirconium phosphate is used as a platform to achieve OER catalysis within confined environments, where a definitive interlayer spacing provides for catalysts to be developed with high activity and stability. We show that the intercalation of Ni and Fe cations within θ-zirconium phosphate modulates the homogeneity of the interlayer spacing as a function of cation loading and produces three distinct intercalated phases. Fully intercalated systems are shown to have an improved intrinsic activity when normalized to their mass, in relation to adsorbed counterparts, and an optimum is revealed for an Fe-rich intercalated (I-$Ni_{0.1}Fe_{0.9}$) catalyst, particularly interesting as Fe-rich catalysts are not viewed as optimum in more conventional catalyst formats. By means of studies coupling XRD, ICP-MS, and chronopotentiometry, we verify that the catalytic species confined within the interlayer are stable. Using octadecyl isocyanate (ODI) to displace surface bound (adsorbed) Ni/Fe species from I-$Ni_{0.1}Fe_{0.9}$ catalyst, we demonstrate that the majority of the OER activity originates from Ni/Fe species intercalated within the structure, rather than at the outer surface. Computationally, we explore a number of intercalated structures for their stability and activity and identify phosphate groups as the main anchoring sites. The confined environment provided by zirconium phosphate improves activity (on both a geometric and mass basis), effects arising from various factors, including perturbations to the water environment within the confined interlayer as well as the tunability of the cation composition that changes the nature of the active site. This work shows the promise of layered materials with phosphate groups as an emerging platform to confine catalytic species, leading to physical and chemical effects that can be leveraged for increased performance for a variety of chemical reactions.

Results and Discussion:

Adsorbed and Intercalated Zirconium Phosphate Structures

α-Zirconium phosphate (**Figure 1A**) is a non-precious-metal layered material that consists of zirconium atoms octahedrally coordinated with oxygen atoms of bridging phosphate groups. The three oxygens of each phosphate group bridge three different zirconium atoms in a corner-sharing fashion. The fourth and non-bridging oxygen of each phosphate group is bonded to an acidic exchangeable proton. Ion-exchange of this proton, located above and within the layers with other cation species enables the modification of the surface acidity, hydrophobicity/hydrophilicity, textural properties, and changes in interlayer spacing making zirconium phosphate highly versatile and useful for numerous applications.[48] The layer spacing can also be controlled simply by changing the number of interlayer waters between the sheets. The *α*- and *θ*-$Zr(HPO_4)_2 \cdot nH_2O$ phases (**Figure 1B**, with n=1 and n=6 for the *α* and *θ* phases, respectively) have been the most highly studied polymorphs and their interlayer distances are 7.6 Å and 10.4 Å, respectively.[49] When intercalated with different ions, structural changes have been observed for intercalated derivatives of zirconium phosphate and these changes disrupt the standard orientation of the phosphate groups and interlayer spacings. [50,51]

It is known that the *α*- phase's interlayer distance of 7.6 Å is too small to intercalate cation species with a ionic diameter larger than 2.61 Å without additional techniques such as solvent exchange, sonication, heating, or additional energy into the system to overcome the intercalation threshold barrier.[33,42,43,52] The *θ*-phase, on the other hand, with an interlayer distance of 10.4 Å (due to six interlayer water molecules per formula unit) readily allows for the direct intercalation of larger positively charged species. In this work, we utilize the *α*- and *θ*- zirconium phosphate phases to strategically synthesize surfaced adsorbed (Phase 0, using the *α*-phase) and interlayer intercalated

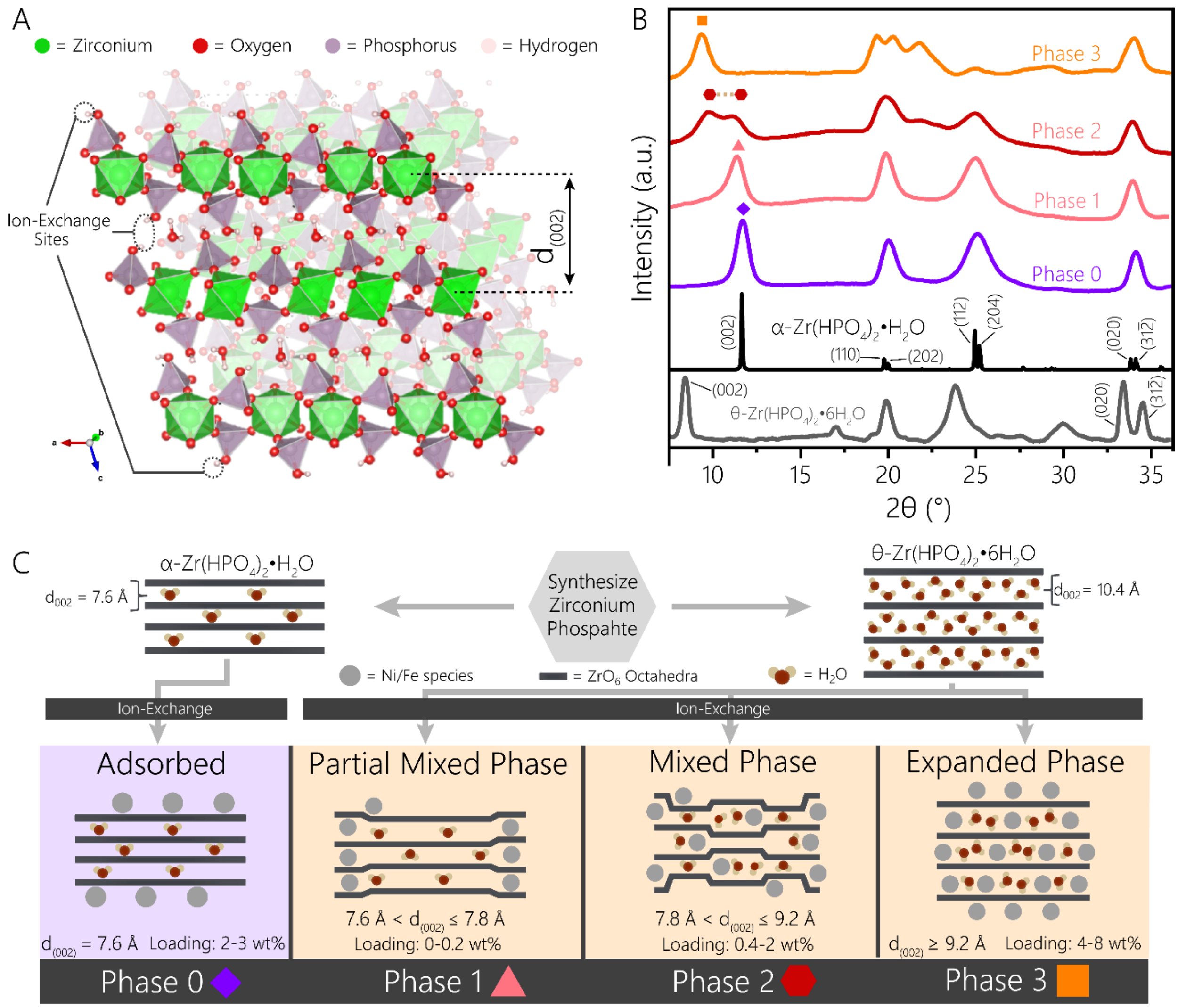

Figure 1 – (A) Crystal structure of *α*-zirconium phosphate (ICSD 1281) where ZrO_6 octahedra (green) are linked to phosphate tetrahedra (gray). Interlayer distance for the (002) reflection is characterized by the distance between Zr atoms in opposite layers and is altered by the amount of interlayer water and/or intercalated species. Ion-exchange of cations occurs at the exchangeable protons (dashed circles) found within the interlayer and on the outer surfaces of the zirconium phosphate nanoparticles. In this schematic, only a select few protons are encircled whereas the sites of ion exchange occur throughout the layered material. (B) Representative X-ray diffraction patterns of the *α*-phase (ICSD 1281), the experimentally collected *θ*-phase, and the four synthesized phases at a Fe/(Fe+Ni) composition of ~90%. (C) Schematic illustration of the synthesis process for intercalated and adsorbed zirconium phosphate systems. Purple and orange backgrounds correspond to the *α*-phase and the *θ*-phase undergoing ion-exchange to form adsorbed and intercalated Ni/Fe catalyst systems, respectively. Four different systems are produced from two zirconium phosphate phases, *α*- and *θ*-zirconium phosphate, and are subdivided into adsorbed (Phase 0) and intercalated (Phage 1-3) systems, respectively. For intercalated systems, the three different phases correspond to the different mixing of *θ*-zirconium phosphate as a function of increasing cation (Ni + Fe) loading (relative to total catalyst loading). Dark gray lines represent the (002) planes of zirconium phosphate where the interlayer distance (d_{002}) ranges from 7.6 to 10.4 Å)

catalysts (Phases 1-3, using the θ-phase) with a range of Ni/Fe compositions. To synthesize this broad set of catalysts, we systematically vary cation loading by modifying the concentration and molar ratio of the metal salt precursors relative to the zirconium phosphate host material. We employ X-ray diffraction (XRD) to observe the extent of intercalation, compared to the control α- and θ- phases, by tracking the lowest angle (002) peak (**Figure 1B)**. A schematic of the different phases synthesized is depicted in **Figure 1C**. Furthermore, transmission electron microscopy (TEM) micrographs showcase no distinct morphological differences between the four systems (**Figure S1**). Catalysts with various Ni/Fe ratios adsorbed to the surface are synthesized using α-zirconium phosphate as a starting material (**Figure 1C**, Phase 0). The absence of intercalation is confirmed through XRD (**Figure 1B**) which shows a pattern consistent with an α-zirconium phosphate that has an interlayer distance of 7.6 Å. As described above, the Ni and Fe cations are unable to diffuse within the layers and thus, the ion-exchange of cations occurs only on the bridging phosphate groups of the outermost surface of the nanoparticles.

Co-intercalated catalysts are synthesized from the θ-zirconium phosphate precursor. In these syntheses, the Fe and Ni ions can adsorb both onto the surface of the material as well as intercalate into the θ-zirconium phosphate structure (**Figure 1C**, Phase 1-3 (P-1, P-2, and P-3)). By modulating the total Ni/Fe cation loading during the ion-exchange process, while keeping the amount of θ-zirconium phosphate constant, we synthesize three unique phase mixtures of intercalated Ni/Fe zirconium phosphate that vary by the degree of interlayer expansion. Degree of expansion is characterized by a shift in the (002) peak or by the appearance of multiple peaks at 2θ values lower than 11.5°. Based on previous reports, at low loadings, the introduction of cation and water species occurs initially at the edges of the zirconium phosphate sheets by the removal or partial removal of the solvation shell of a positively charged species.[53] Once removed, the intercalating species can enter through the edges of the zirconium phosphate layers (P-1) causing an expansion of the edges. Specifically, P-1 systems shows expansion of up to 0.2 Å compared to the parent α-zirconium phosphate phase. This slight expansion, observed concurrently with the broadening of the (002) peak, indicates that species are introduced to the outermost galleys of the zirconium phosphate sheets thus expanding the edges of the interlayer.[53] At intermediate loadings, diffusion of the positively charged species is hypothesized to occur from the edges towards the center of the galleries (P-2). As seen in the diffractograms, the layered structure in the P-2 systems is highly perturbed showcasing two distinct peaks between 7.8 and 9.2 Å – one at approximately $2\theta \approx 11.5^{o}$ and another at lower 2θ values (9.5-9.8°) indicating that a mixed phase with partial (P-1) and near full layer expansion (P-3) is present. The left most peak is indicative of a new intercalated phase that is not yet fully expanded while the right most peak is representative of the parent α-zirconium phosphate structure with slight expansion. Finally, at high loadings, the insertion of additional species is expected to manifest in the formation of new bonds that drives the diffusion of cations to move further into the channels until the layers of the zirconium phosphate are fully expanded (P-3). Indeed, P-3 systems display a shift of the 002 peak to lower 2θ values (9.4-9.6°) and no peak at ~7.6 Å, as expected for a pure fully expanded intercalated phase material. Characteristic diffractograms for all phases are shown in **Figure S2** as a function of increasing Ni/Fe content and are shown to exhibit similar diffractograms as described above. The confirmation of various distinct phases of Ni/Fe zirconium phosphate systems through XRD enables the assessment of composition, structure, interlayer distance, and loading on performance for the OER.

Structure, Conductivity, and Activity for Ni/Fe-modified Zirconium Phosphate Catalysts: Ni/Fe Adsorbed on the Surface and/or Intercalated Within the Layers

To probe electrochemical OER activity as a function of Ni:Fe composition and confinement, the prepared suite of adsorbed (P-0) and intercalated (P-1, P-2 and P-3) catalysts were evaluated using cyclic voltammetry. Towards rationalizing observed activity trends, we evaluated the as-prepared interlayer spacing, conductivity, and OER performance assessed through the overpotential for the OER at 10 mA cm^{-2} (η_{10}) and mass activity at an overpotential of 350 mV (M.A.$_{350}$) for a large Fe:Ni compositional range (**Figure 2**). Both performance metrics are from the average of a forward and reverse sweep (1st cycle) of the voltammograms (10 mV s^{-1}) in 0.1 M KOH. **Table S1** details all the values depicted in **Figure 2**.

As described in detail previously, the interlayer distance varies with the extent of Ni/Fe cation intercalation to create four unique phases. The various phases were accessed by modulating either the starting layered structure (P-0 vs P-1−P-3) or cation loading (P-1−P-3). **Figure 2A** (full diffractograms are shown in Figure S1A-D) shows the interlayer spacing as function of the Ni:Fe ratio. For each phase, we see minimal changes in interlayer distance across the compositional ranges indicating that interlayer spacing is not composition dependent. This allows for the comparison of activity within each phase across compositions without the influence of a variable interlayer distance. **Figure 2B** displays the four-point probe conductivity measurements assessed for the catalysts powders (prior to electrochemistry) as a pressed pellet. **Figure 2B** shows that as the Fe content increases from 0 to 100%, all catalyst systems show a noticeable decrease in conductivity by 1-2 orders of magnitude. Nearly all systems show reduced catalyst conductivity as a function increased Fe content, both absolute or measured relative to Ni and Fe wt% (**Figure S3A**) as compared to *α*-zirconium phosphate (black dashed line). Based on previous in situ conductivity reports, we hypothesize that the Fe content readily converts to iron oxide species leading to a more insulating catalyst.[54]

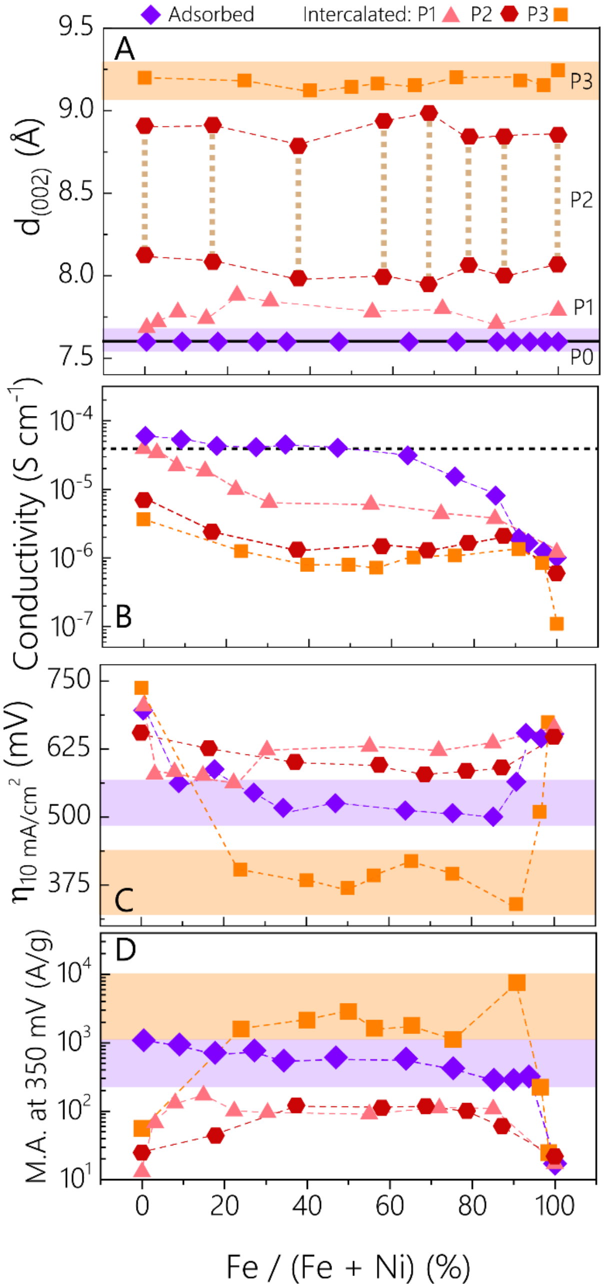

Figure 2 - Ni-Fe compositional dependence on **(A)** interlayer distance obtained for the (002) plane of zirconium phosphate from XRD measurements. Solid black line represents the interlayer spacing of α-zirconium phosphate. **(B)** Four-point probe conductivity measurements. Black dashed line represents the four-point probe conductivity of α-zirconium phosphate. **(C)** overpotential for the OER (relative to 1.23 V vs. RHE) at 10 mA cm^{-2} in 0.1 M KOH, and **(D)** mass activity at 350 mV for adsorbed (purple diamonds) and intercalated (P-1: salmon triangles, P-2: red hexagons, P-3: orange squares) Ni/Fe zirconium phosphate catalysts. Purple and orange and highlighted regions emphasize

To understand the role of activity enhancement as a function of spacing, we compared η_{10} (**Figure 2C**) and M.A.$_{350}$ (**Figure 2D**) at all Ni/Fe ratios and phases. Specifically, η_{10} assesses activity on a geometric basis, which can be dependent on catalyst loading, while M.A.$_{350}$ provides an intrinsic activity assessment by normalizing to the total cation mass obtained from ICP-MS. The M.A.$_{350}$ is particularly important since improved activity can be correlated with an increased loading of Ni and Fe species within P1- P-3 systems with P-3 systems having the highest Ni/Fe loading **(Figure S3B)**. It is important to note that the M.A. is also likely an underestimation of activity as it assumes that all Ni/Fe cations are active. By both metrics, consistent with previous experimental reports, all systems, on average, have enhanced mixed Ni/Fe performance in relation to the elevated η_{10} and reduced M.A.$_{350}$ for monometallic systems.[44–47]

For adsorbed (P-0) systems, pure Ni and Fe compositions exhibit high η_{10} of 695 and 592 mV and M.A.$_{350}$ values of 1025 and 120 A/g, respectively. As the amount of Fe content relative to Ni increases (0 to 9 %), there is an initial improvement of ~ 130 mV. Increasing the Fe ratio up to 85% further reduces the overpotential to a minimum ~ 500 mV. However, once the Fe content surpasses 90%, η_{10} is negatively impacted as observed by the η_{10} = 592 mV at 100 % Fe content. Furthermore, when assessed for M.A.$_{350}$, P-0 systems exhibits a two orders of magnitude reduction in M.A$_{350}$ (1088-12 A/g) from 0 to 100% Fe content relative to Ni. For intercalated systems, improved η_{10} based on Ni/Fe synergism are observed for Ni/Fe P-1 (low-loading) and P-2 (intermediate-loading) systems. However, compared to the adsorbed system, both P-1/P-2 systems, on average, have worse performance than P-0 by ~50 mV and ~600 A/g on a M.A.$_{350}$ basis. Coincidentally, P-1 and P-2 also have an order of magnitude lower conductivity than the adsorbed (P-0) systems which could indicate that their poor performance is due to inhibited electron transfer through the zirconium phosphate sheets. In contrast, the high-loading fully expanded systems (P-3), show improved η_{10} by an average of ~ 100 mV and ~ 150 mV compared to adsorbed (P0) and P-1/2 systems, respectively at all mixed Ni/Fe compositions. In terms of M.A.$_{350}$, P-3 systems, on average, are ~3 times more active on a mass basis compared to adsorbed systems (~ 2400 vs. ~ 740 A/g, respectively) at similar compositions and are an order of magnitude more active than P-1/2 systems (~ 2400 vs. ~110 A/g, respectively). This analysis indicates that among all the unique interlayer environments made possible from the different phases synthesized

(P-1−P-3), the most active catalysts involved interlayer spacings characteristic of the P-3 systems with intercalated, mixed Ni/Fe cations of a high Fe content.

Computational studies have indicated that an optimal interlayer spacing can favorably impact metal-adsorbate binding energies and enhance activity.[23] We hypothesize that the interplay between the optimal interlayer spacing and Ni/Fe composition in the P-3 systems may be responsible for the improved performance relative to the adsorbed systems. An improvement in activity is not universally observed for confined metal species within zirconium phosphate at a similar interlayer spacings and loadings when compared to adsorbed counterparts.[44] This nonuniversal trend indicates that the active site environment and cation composition in confined (P-3) mixed Ni/Fe compositions (**Figure S3C**) is unique. To further investigate this observed phenomenon, we examine the differences between the most active intercalated composition (P-3, 90% Fe content relative to Ni, $\eta_{10} = 340\,mV$) and its adsorbed (P-0, $\eta_{10} = 655\,mV$) counterpart.

Elucidating Surface versus Confined Catalysis: An Activity and Stability Assessment for Adsorbed and Intercalated $Ni_{0.1}Fe_{0.9}$ Catalyst Systems

Majority of Ni/Fe Species Remain within the Zirconium Phosphate Layers during Catalysis.

Before probing the root of the intercalated enhancement, we first assessed the material stability and the longevity of the Ni/Fe species during catalysis either within the layers or adsorbed on the surface (**Figure 3**). As clarified previously, fully expanded P-3 intercalated catalysts outperform adsorbed P-0 catalysts for all mixed Ni/Fe compositions. Interestingly, we see that the most active intercalated P-3 compositions range between 28 – 90 % Fe with a maximum at 90 % Fe, labeled as I-$Ni_{0.1}Fe_{0.9}$, P-3 in **Figure 3A**. Due to its enhanced activity and high Fe content, we focus on this composition for our in-depth stability and intrinsic activity. To assess the change in metal loading, the amount of catalyst that is responsible for the OER current, and gauge the integrity of the layers during catalysis, I-$Ni_{0.1}Fe_{0.9}$ intercalated (P-3) and adsorbed (A-$Ni_{0.1}Fe_{0.9}$, P0) systems were monitored after cyclic voltammetry, by ICP-MS and XRD, respectively (**Figure 3A-C**).

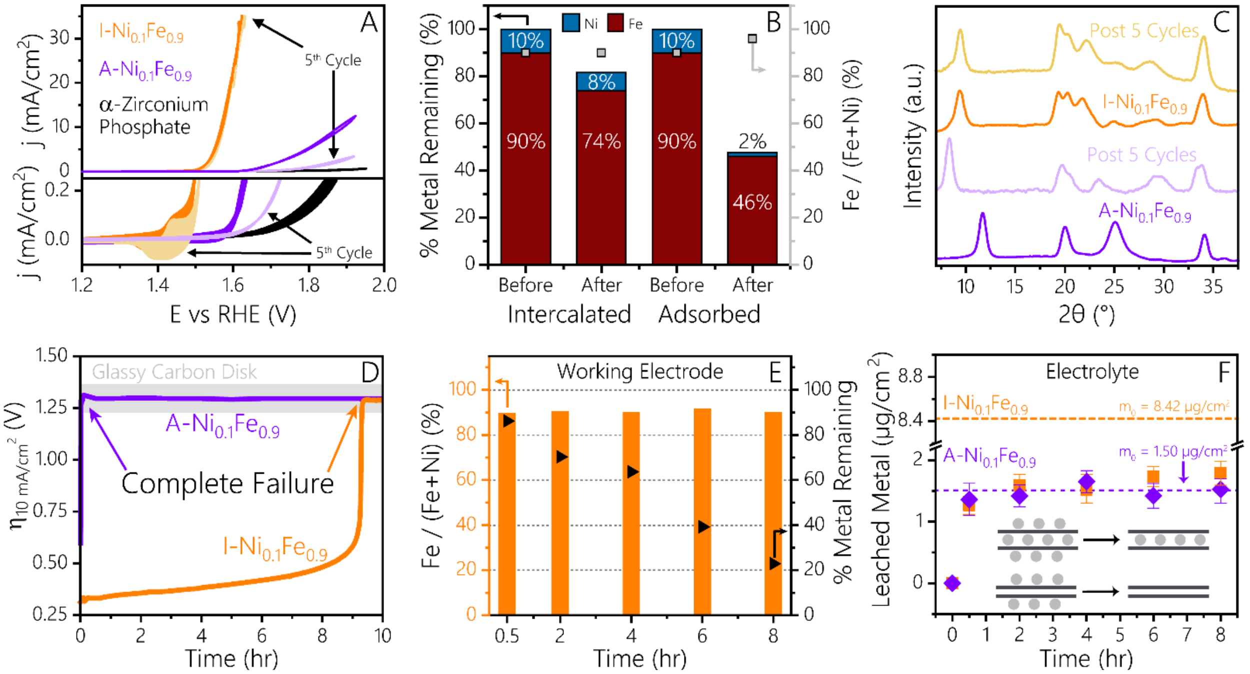

Figure 3 – Electrochemical stability studies for adsorbed and intercalated Ni$_{0.1}$Fe$_{0.9}$ catalysts in a 0.1 M KOH electrolyte. (A) Cyclic voltammetry of adsorbed and intercalated Ni$_{0.1}$Fe$_{0.9}$ catalysts showing the first and fifth cycle. The 1st cycle is shown in orange (I-Ni$_{0.1}$Fe$_{0.9}$) and purple (A-Ni$_{0.1}$Fe$_{0.9}$) while the fifth cycle is shown in a lighter color in comparison to the original 1st cycle. Inset plot below shows the redox features exhibited by the I-Ni$_{0.1}$Fe$_{0.9}$ catalyst in the same potential window as the above panel with the same legend. Corresponding plots of the amount of (B) metal remaining on the working electrode (left axis) and final composition (right axis – gray squares) after five cycles through ICP-MS analysis. (C) XRD of the adsorbed and intercalated Ni$_{0.1}$Fe$_{0.9}$ catalysts after five cycles. (D) Chronopoteniometry of adsorbed and intercalated Ni$_{0.1}$Fe$_{0.9}$ catalysts. The light-gray shaded region represents the overpotential range exhibited by a pristine glassy carbon disk to achieve η_{10}. (E) Corresponding plots of Fe / (Fe + Ni) composition and remaining metal on the working electrode for an intercalated Ni$_{0.1}$Fe$_{0.9}$ catalyst. (F) ICP-MS analysis of the electrolyte quantifying the amount of leached metal (Ni and Fe species) for adsorbed and intercalated Ni$_{0.1}$Fe$_{0.9}$ catalysts during chronopotentiometry. Schematic within the panel represents a possible interpertration of the leached metal data where adsorbed species dissolve from the outer surface of both A- and I-Ni$_{0.1}$Fe$_{0.9}$ catalysts.

By cyclic voltammetry (5 cycles) we see that the I-Ni$_{0.1}$Fe$_{0.9}$ has a significant Ni redox (+2→ +3) feature centered around 1.43 V vs RHE (**Figure 3A**). This feature is common in layered Ni/Fe materials and is observed for all of the mixed-metal intercalated systems (**Figure S4A and C**).[9] Furthermore, after 5 CVs, the activity, nickel redox features, Ni/Fe ratio, Zr/P ratio, and interlayer spacing remain relatively constant. (**Figure 3A-C and Figure S5**). Specifically, the η_{10} at the fifth cycle is 8 mV higher when compared to the first cycle. By digesting the working electrode in aqua-regia after the moderate electrochemical cycling we were able to monitor the Ni and Fe species remaining after catalysis via ICP-MS. We see ~20% total losses in Fe and Ni species for the I-Ni$_{0.1}$Fe$_{0.9}$ catalyst and it retains its as prepared composition of 90% Fe. This retention of high Fe content is particularly interesting because typically high Fe-containing catalysts have been seen to disproportionally dissolve Fe due to FeO_x phase segregation.[54] There have been increasing concerns that some of the current we have attributed to OER is actually from metal dissolution or carbon corrosion.[55–57] For this reason, we examined the possibility as to whether part or all of current observed during the first cycle could originate from Fe or carbon corrosion. Based on our calculations (**see SI for details**), total Fe or carbon corrosion would correspond with ~ 0.74% and ~ 104% of the total charge passed during the first cycle, respectively. For Fe, because total dissolution would impact < 1 % of the current it is unlikely that Fe corrosion contributes substantially to the observed current. Furthermore, the lack of impact on the current from C corrosion is showcased by the intercalated current stability over 5 cycles (a level of stability that would not have been possible if 20 % of the C corroded each cycle). Additionally, as shown in **Figure S6**, if all the C black were to corrode there would be no activity without the conductive backbone. The retention of the majority of the Ni/Fe species, an unperturbed interlayer spacing, and OER stability support the hypothesis that the Ni/Fe species remain within the interlayer during catalysis.

In contrast to I-$Ni_{0.1}Fe_{0.9}$, the cyclic voltammetry for A-$Ni_{0.1}Fe_{0.9}$ shows that the Ni-redox wave is not present in any cycle for the adsorbed catalysts and for all other adsorbed systems (**Figure S4B,D**). This could suggest that the Ni species adsorbed on the surface of the zirconium phosphate sheets are not electrochemically accessible/active or that they do not remain on the surface during electrochemical evaluation. Furthermore, after 5 cycles (**Figure 3A**), we see that the A-$Ni_{0.1}Fe_{0.9}$ lost 87% of its maximum activity (25 to 1.4 mA/cm^2 at 1.8 V vs RHE) and approaches the activity of pristine zirconium phosphate. However, as seen by ICP-MS, the A-$Ni_{0.1}Fe_{0.9}$ only loses ~50 % of its total metal content (**Figure 3B**). There is disproportional Ni-dissolution and the final composition has only 4 % Ni relative to Fe. Notably, the amount (1.4 ± 0.1 μg/cm^2) of Ni/Fe that was lost when the I-$Ni_{0.1}Fe_{0.9}$ was cycled nominally matches the total amount (1.5 ug/cm^2) of species contained by A-$Ni_{0.1}Fe_{0.9}$. We hypothesize that only adsorbed Ni/Fe species dissolve for both systems, likely because intercalated Ni/Fe species are strongly coordinated within the zirconium phosphate sheets, as discussed later in the computational section. It also suggests that the Ni redox as seen by the intercalated catalyst is not from Ni/Fe species adsorbed to the surface. XRD of the cycled catalyst shows an expansion in the interlayer spacing from 7.6 to 10.6 Å. This level of expansion is consistent with a final structure that is similar that of a fully expanded θ-zirconium phosphate. and could be due to either hydration and/or potassium intercalation during the catalysis (**Figure S7-8**). It is interesting to note that the final A-$Ni_{0.1}Fe_{0.9}$ layer spacing is ~1.4 Å larger than that of the I-$Ni_{0.1}Fe_{0.9}$, which remains at a constant interlayer spacing of ~9.2-9.3 Å, suggesting that intercalated Ni/Fe species alter the dynamics of dissolution, hydration, and/or potassium intercalation during catalysis. Despite the poor activity and the lack in redox wave, the slight OER activity above that of zirconium phosphate and the partial retention of Ni/Fe species indicates that that within our moderate cycling of the A-$Ni_{0.1}Fe_{0.9}$ we are indeed probing adsorbed species electrochemically.

To assess the longer-term stability of the I-$Ni_{0.1}Fe_{0.9}$ and A-$Ni_{0.1}Fe_{0.9}$ systems during catalysis we monitored the Ni and Fe content for ~ 8 h at 10 mA/cm^2. The chronopotentiometry (CP) (**Figure 3D**) shows that the A-$Ni_{0.1}Fe_{0.9}$ catalyst rapidly degraded in less than 72 seconds, while the I-$Ni_{0.1}Fe_{0.9}$ was dramatically more stable (by an order of magnitude) with only ~19 mV/hr decay in performance during nine hours of continuous operation. After nine hours we see rapid and complete catalytic failure. This type of catalytic failure has been previously associated with substrate failure.[56,57] ICP-MS analysis (**Figure 3E**) of the working electrode shows that the Fe/Ni ratio remains constant at 90% for the duration of the experiment. However, a loss in the total Ni/Fe content is observed throughout the duration of the experiment. Specifically, at 30 mins, 84% of the Ni and Fe metal content remain on the electrode. As time increases, the amount of metal remaining drops to 65, 61, 39, and 22% for 2, 4, 6, and 8 hours respectively. Analysis of the working electrode (**Figure S9**) indicates that the loss in active mass might be attributed to concomitant carbon corrosion/delamination as well Ni/Fe dissolution. To decouple delamination and dissolution, in conjunction with the ICP-MS analysis of the working electrode, ICP-MS analysis was also performed during the CP via aliquots taken from the electrolyte. Analysis of the Fe and Ni dissolved in the electrolyte (**Figure 3G**) reveals that nearly all the dissolution occurs within 30 min of testing, illustrating that the majority of loss of activity is possibly due to catalysts dissolution. Interestingly, a similar mass dissolution of ~1.50 µg/cm^2 into the electrolyte is shown for the intercalated (P-3) system within 30 minutes for the duration of the experiment. In agreement to previous grafting experiments, the electrolyte analysis indicates that the activity of the I-$Ni_{0.1}Fe_{0.9}$ catalyst occurs mostly within the bulk of the interlayers since an equal mass loss to that of surface bound adsorbed species is found to dissolve during electrochemical testing. Since the carbon is shown to delaminate during testing, it is hypothesized that active material goes into solution and does not dissolve; therefore, we will only see the mass of Fe and Ni species from this delaminated catalyst layer if it chemically dissolves since solids are filtered out during aliquot testing for ICP-MS analysis. This analysis, accentuated by activity, structural, and ICP-MS data, supports the hypothesis that for both systems, adsorbed species dissolve from the outer sheets of zirconium phosphate. This understanding along with the stability of the interlayer allows us to further probe the activity of the confined Ni/Fe catalysts.

Active Ni/Fe Species within the Zirconium Phosphate Layers.

There have been several examples in which a specific local environment plays a deciding role in the properties of an active site.[19,21] Our confined layered Ni/Fe catalysts (P-3) have a unique, well-defined environment and the Ni/Fe species remain within the layers during catalysis. To determine if the origins of the enhanced activity are within the interlayer, we conducted a series of electrochemical experiments (**Figure 4**) focused on probing the kinetics (Tafel plots) and location of active species (surface grafting). In depth analysis of the rate of OER turn-on as a function of overpotential, e.g. Tafel slope, have been used to compare the reaction kinetics of different catalytic materials. A Tafel slope values of the polarization curves (**Figure 4C**) shows that I-$Ni_{0.1}Fe_{0.9}$ not only reduces the onset potential, but also has a substantial lower Tafel slope of 41 mV/dec compared to the 220 mV/dec of A-$Ni_{0.1}Fe_{0.9}$. The Tafel slope of 41mV/dec is particularly interesting since it is similar to that of a layered double hydroxide (LDH) system suggesting the same rate limiting step (RLS). [9] However, these values are commonly obtained for a Ni-rich Ni/Fe LDH system, and not for the Fe-rich system reported here. A similar Tafel slope could also indicate that a similar catalytic motif to that of a LDH has been made within the confined space of zirconium phosphate sheets albeit at a high Fe content, as discussed later in the computational section. Furthermore, a reduced Tafel slope (**Figure S10**) is found to only common to the mixed metal P-3 systems as opposed to P0 ones.

In order to determine if the confined Ni/Fe species are catalytically active in the interlayer during catalysis, the performance and electrochemical profile of A- and I- $Ni_{0.1}Fe_{0.9}$ catalysts were compared after displacing surface-adsorbed Ni/Fe species (**Figure 4D-F**). In this case, with surface catalytic sites displaced, any activity would be due to intercalated species. To remove the surface

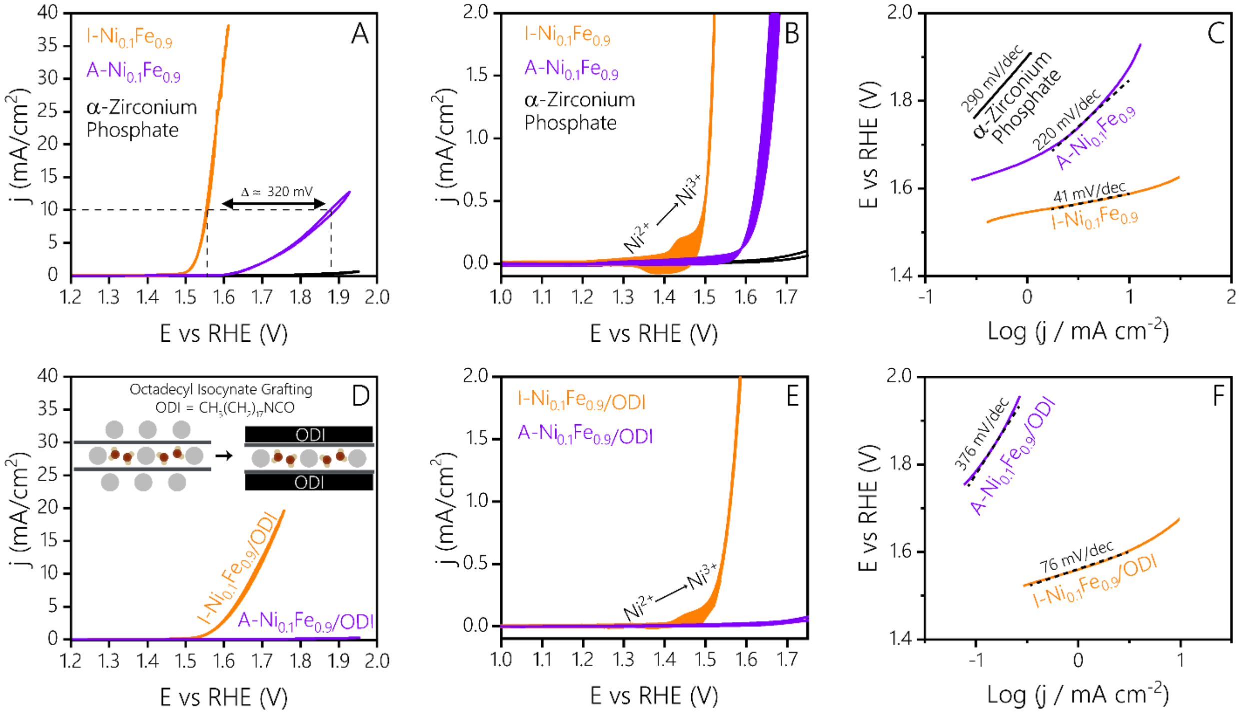

Figure 4 – Cylcic voltammetry studies for **(A)** adsorbed (purple) and intercalated (orange) $Ni_{0.1}Fe_{0.9}$ catalysts and **(B)** zoomed in view of panel A to showcase the Ni redox feature. **(C)** Tafel plots for adsorbed and intercalated $Ni_{0.1}Fe_{0.9}$ catalysts. **(D)** Cyclic voltametry studies for ODI modified adsorbed and intercalated $Ni_{0.1}Fe_{0.9}$ catalysts and **(E)** zoomed in view of panel D to showcase the Ni redox feature. **(F)** Tafel plots for ODI modified adsorbed and intercalated $Ni_{0.1}Fe_{0.9}$ catalysts.

sites we synthesized A- and I- $Ni_{0.1}Fe_{0.9}$ catalysts as described above, subsequently grafted with octadecyl isocyanate (ODI) following literature protocol,[58] and assessed for the OER. Successful grafting, resulting in the displacement of surface bound metal species, was confirmed through the electrochemical inactivity of the ODI-modified A-$Ni_{0.1}Fe_{0.9}$ catalyst (**Figure 4D**). Conversely, for the intercalated ODI-modified catalyst, electrochemical activity is modestly reduced and the Ni redox remained apparent (**Figure 4E**). These findings suggest that 1) the species at the interlayer are active for the OER and 2) Ni-based species remain electrochemically accessible within the interlayer. The catalytic performance of the grafted I-$Ni_{0.1}Fe_{0.9}$ is lower than that of the non-grafted system and the Tafel slope (**Figure 3F**) of I-$Ni_{0.1}Fe_{0.9}$ /ODI is ~ 2x higher than its' non-grafted counterpart. We postulate that this observed difference in activity could stem from hindered water transport to the interlayer due to the hydrophobic ODI molecules grafted to the surface of zirconium phosphate. To our knowledge, this is the first time where it has been clearly shown that the interlayer is active for the OER for confined layered catalysts. To investigate the interlayer enhancement, assessments on the systems structure (DFT calculations), composition (Fe oxidation), and environment (water content) are presented below.

Computational Analysis of the Intercalated Zirconium Phosphate Structure

In order to investigate the structural identity and activity of the confined motif within the interlayer of zirconium phosphate, DFT and a thermodynamic approach to the OER were employed. As expected from the ion-exchange chemistry of zirconium phosphate, our calculations find that removal of the exchangeable proton at the OH of the phosphate group is necessary for any bond formation to occur with the layers. Based on the available crystal structures within the literature and the ICSD database, we have identified wycheproofite, $NaAlZr(PO_4)_2(OH)_2{\cdot}H_2O$ (ICSD:55430) as a host platform to simulate P-3 catalysts (**Figure 5**).[50,59,60] This host platform allowed for a stable octahedral configuration of intercalated 3+ cations. Other coordinations, tested only for α-phase are shown in **Figure S11**. Specifically, when octahedral Al^{3+} is substituted by Fe^{3+}/Ni^{3+}, the fully optimized structure has very similar XRD features as the I-$Ni_{0.1}Fe_{0.9}$ catalyst (**Figure 5A**), which remains unchanged for other simulated Fe/(Fe+Ni) ratios (**Figure S12)**. We assume that Fe^{3+} can occupy Al^{3+} sites as its often observed for earth crust crystals and for NiOOH systems.[61,62] Molecular dynamics showcase Fe ion adsorption on inner layers of Ni/FeOOH, which result in a similar octahedral intercalation motif.[63] Additionally, as shown in **Figure S7**, replacement of Na^+ with K^+ is possible due to intercalation of solvated K^+ species from KOH electrolyte. The resulting wycheproofite-type structure ($K(Ni_xFe_{1-x})O_2\ Zr(HPO_4)_2{\cdot}H_2O$, **Figure 5B**) with an interlayer distance of 8.9 Å features octahedral zig-zag chains of intercalated Fe^{3+} and Ni^{3+} cations connected to zirconium phosphate layers via two phosphate groups per cation, similar to that observed in bulk olivine-type $Li(Fe/Ni)PO_4$.[64] While there is high correlation between the observed XRD features and simulated structure, we note that this structure is one possible representation of Ni and Fe species within the interlayer of our catalyst. Nevertheless, the simulated structure represents a good model for octahedral bonding of cations within the interlayer where bonding occurs via phosphate groups.

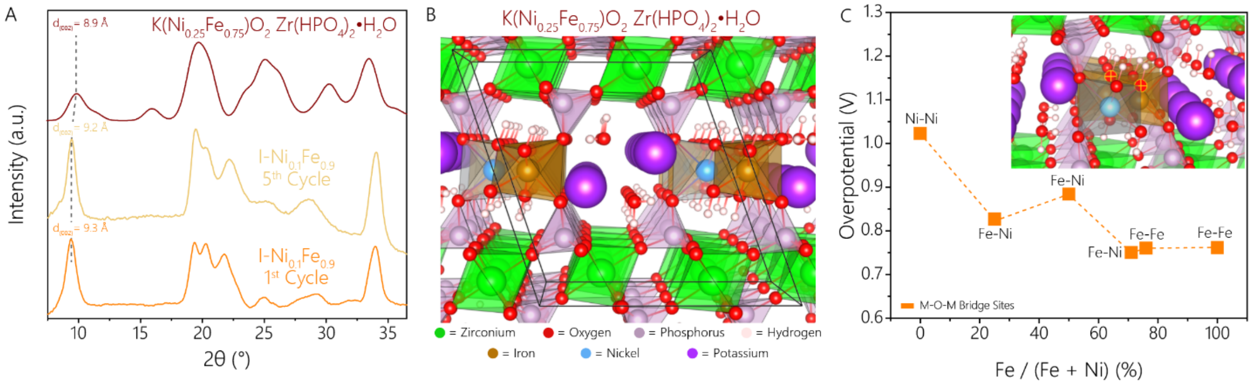

Figure 5 – **(A)** Comparission of the XRD patterns fo the simulated $K(Ni_{0.25}Fe_{0.75})O_2$ $Zr(HPO_4)_2{\cdot}H_2O$ (dark red) with the meassured intercalated I-$Ni_{0.1}Fe_{0.9}$ catalyst after 1 and 5 cycles (orange and yellow, respectively). For direct comparison with experiemnt, a gaussian broadening was of applied to calculated XRD. The corresponding XRD paterns for other Fe/(Fe+Ni) ratios are shown in **Figure S12** **(B)** Detailed view of simulated wycheproofite structure $K(Ni_{0.25}Fe_{0.75})O_2$ $Zr(HPO_4)_2{\cdot}H_2O$ highlighting the chains (Fe/Ni)O_6 octahedra bonding (orange/blue) to tetragonal PO_4 groups (purple). **(C)** Calculated trends in the OER activities based on the structure (B) as fucntion of the Fe/(Fe+Ni) ratio. The metal-O-metal (M-O-M) bridge activity of the bulk-sites trend is shown as orange squares, with labels indicating the type of the metals in the bridge. Inset on the top-right correponds to a zoom in of the panel shown in (B) with highlighted (yellow circle outline) oxygen active sites.

The theoretical activities of the bulk sites within the simulated structure were assessed from calculated adsorption thermodynamics of OH*, O* and OOH*.[65–67] In our analysis, Zr^{+4} and PO_4^{-3} sites were calculated as inactive towards OER, acting as strong Lewis acid pairs to oxygen's Lewis base. In **Figure 5C**, we highlight the calculated trends in OER activity as function of the Fe-Ni ratio. Specifically, we assess the activity of M-O-M bridge sites which feature double coordinated oxygen (O_{2c}) in the octahedral chains of the simulated bulk structure. Our results show that presence of Fe next to Ni (Fe-O-Ni bridge sites) is beneficial for the OER activity, reducing the OH* to O* potential limiting step (PLS) for Fe-Ni mixtures. The origin of this effect is mostly electronic, where high-spin Fe^{+3} binds O_{2c} much stronger than low-spin Ni^{+3}. Similar results are found with top-site binding in NiFeOOH studies, which is combined with minor structural effect, where the Fe^{+3} cation with larger ionic radius expand the lattice relative Ni^{+3} cation.[65,68,69] The local minimum in overpotential is achieved for Fe-O-Ni at 75% Fe content, which agrees well with the results observed for P-3 systems (**Figure 2C,D**). The calculations for Fe-O-Fe bridge sites with 100% Fe also indicate high activity, though experiments for this system show low conductivity (**Figure 2B**) and instability (**Figure S9**) compared to Ni-containing rich P-3 systems.

Trends in our octahedral intercalation model are consistent with observed experimental trends. To further understand the variability within the system theoretically we probed the role that modifying other factors such as K^+ removal, surface activities at phosphate, and metal terminated (001) surfaces play in lowering the overpotentials from bulk intercalated values (~0.8 V). While these structures are not accessible thermodynamically with our current synthesis, theoretically, we show that replacing the PO_x groups with Fe could be an interesting method for improving the activity (**Figure S13 A,B)**. Furthermore, there are additional influences in the intercalated system that arise from a confined catalyst environment, including the effect of water and the electronic structure of the Ni/Fe network that can have a role on the observed activity trends. To that end, we extend our experimental understanding of the possible effects that may influence activity within the confined space by assessing the interlayer through x-ray absorption spectroscopy and thermogravimetric studies.

Interlayer Environment is Important for Enhancement.

The assessment of composition, loading, conductivity, structure, activity, and leaching for the I-$Ni_{0.1}Fe_{0.9}$ catalyst has shown that intercalated species are active and responsible for the majority of the observed OER activity. It is clear that composition and interlayer environment provided by P-3 systems are important in both stabilizing and activating Ni/Fe species within zirconium phosphate. Therefore, to expand on experimental and DFT studies where a high Fe content achieves high activity, we further assessed how confinement of Ni/Fe species could affect the interlayer environment (interlayer water) and/or Ni/Fe properties (oxidation state). Specifically, we find experimental evidence that an elevated Fe oxidation state and an optimum of interlayer water content correlate with improved activity (overpotential and mass activity, respectively) for P-3 systems.

A large body of work has found that Fe exists at an elevated oxidation state and ex-situ and operando measurements have found +3, +4, and +5 oxidation states for Fe-based catalysts. [10,65,70–72] Furthermore, Fe has also been linked to the enhanced electrocatalytic activity observed in these systems.[65,73,74] Thus, we measured Fe-L edges through x-ray absorption spectroscopy (XAS) for as-prepared P-3 catalyst powders and assessed their Fe^{3+} content with activity trends. XAS measurements (**Figure S14A**) show both Fe^{2+} and Fe^{3+} within the spectrum and give insight regarding the electronic interactions between Ni and Fe.

The integral Fe $L_{2,3}$-edge white-line intensity ratios were used to quantify the total number of ferric (Fe^{3+}) iron content for as-prepared intercalated P-3 systems.[75] For these catalysts systems, η_{10} (**Figure S15**) is shown to improve with an increase in Fe^{3+} content while a slight optimum is obtained for mass activity (**Figure S14B**). Specifically, the two intercalated catalysts I-$Ni_{0.1}Fe_{0.9}$ and I-$Ni_{0.5}Fe_{0.5}$ with the lowest η_{10} (340 and 370 mV, respectively) exhibit the higher Fe^{3+} wt% suggesting that Fe^{3+} is important for activity (**Figure S15C)** and higher Fe^{3+} content is observed with increasing Fe content in P-3 systems (**Figure S15D**). Furthermore, when comparing an adsorbed to an intercalated system (**Figure S16**), we find that for I-$Ni_{0.1}Fe_{0.9}$ catalyst, Fe exists at higher ferric concentrations (80%) versus an A-$Ni_{0.1}Fe_{0.9}$ (69%) or an I-Fe (63%) system. Additionally, when comparing Ni-L edges (**Figure S17**), an increase in Fe content leads to an increase in Fe^{3+} content and reduced Ni species indicating a partial electron transfer Fe to Ni and that the interlayer environment plays a role in modulating the oxidation state of the intercalated species.

With regards to the role that the environment plays in enhancing catalysis, molecular dynamic simulations have shown that confined spaces can create frustrated solvation structures (partial solvation shell) such as frustrated water, that have a profound effect on electron transfer through enhanced energy gap fluctuations beyond those expected from Marcus theory.[17,27,76] Zirconium phosphate is a model system to use as a platform to confine Ni/Fe species within the interlayer since it is well known that negatively charged zirconium phosphate sheets interact strongly with water, competing with its hydrogen-bond network.[53] Due to the abundant number of interlayer cations and the confined space within the interlayer of zirconium phosphate which does not allow for a full solvation shell, the solvation shell of water surrounding Ni and Fe species would potentially result in a partial solvation shell. This partial solvation shell is known as frustrated water and has shown enhancements in electron transfer within catalyst materials.[17,76] While the structure/order of water in layered materials can be assessed through neutron diffraction/scattering studies,[77,78] distinct types of water (free vs. bounded water) can also be identified through thermogravimetric analysis (TGA) of the as-prepared zirconium phosphate catalyst powders.[53]

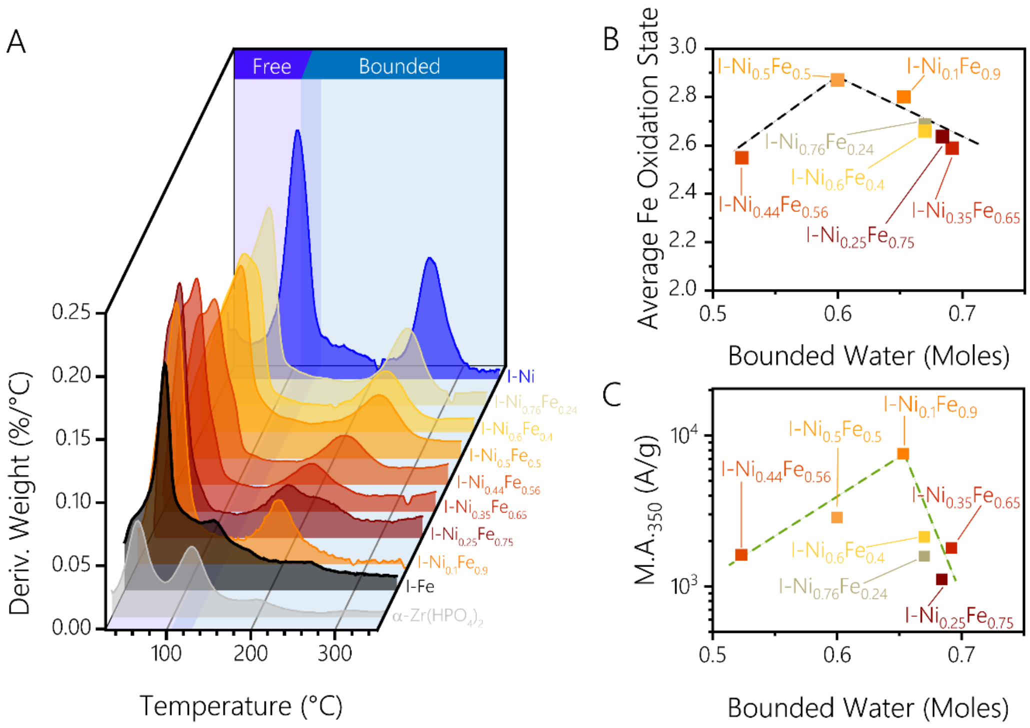

Figure 6 – (A) TGA measurements under N_2 flow showcasing the derivative of the weight loss with respect to temperature for intercalated catalysts as a function of Fe % relative to Ni. **(B)** respective average Fe oxidation state and **(C)** M.A. at 350 mV overpotential as a function of moles of bounded water.

In TGA measurements, the removal of weakly coordinated water (free water) is associated with the first dehydration event and is usually observed below 90-120 °C. The second dehydration event that occurs at higher temperatures and corresponds to strongly coordinated water (bounded water) and herein is considered to be frustrated. **Figure 6A** shows two distinct weight loss regions for all intercalated systems and are shown as separate panels in **Figure S18A-H** for clarity. The total water content of intercalated samples (**Figure S18I**) is found to be between 2.3-2.7 moles of water per mole of zirconium and is similar to previous reports of intercalated metal systems.[79] In terms of activity, an optimum for performance is found with respect to overpotential and mass activity (**Figure 6C**) for bounded water at 0.65 moles of water per mole of zirconium. As the total bounded water increases above 0.65 moles of water per mole of zirconium, it is possible that a more complete solvation shell forms which might mitigate the effect of improved electron transfer.[17,18] XAS and TGA data shows that a specific oxidation state correlates with a specific amount of bounded water (or vice versa) and high activity. We hypothesize that the composition (including oxidation state) of the intercalated structures and the amount of bounded water play a role in controlling the activity of the catalysts (**Figure 6B and Figure S19**) due to an optimum observed for the average iron oxidation state and bounded water. However, we note that these systems are inhomogeneous within the interlayers due to the absence of a trend when comparing composition to iron and water content (**Figure S20**); therefore, decoupling water content and oxidation state is necessary to further understand how the bulk properties of P-3 systems are affected by the co-intercalation of Ni and Fe cations. Additionally, future studies such as dehydration studies for the removal of water and its dependence on Fe^{3+} content and activity, which are out of the scope of this work, would be necessary to elucidate these dynamics during operando conditions. This new understanding of the role of environment (frustrated water) and cation properties (oxidation state) could be used in the future to modify future reactions in confined spaces. Specifically, highly hydrated cations that strongly retain water and that are catalytically active for the OER (Ni^{2+}, Co^{2+}, Fe^{3+}) along with cations that strongly retain water but are not catalytically active (Al^{3+}, Cr^{3+}, Ga^{3+}, Be^{2+}, Mg^{2+}) are interesting species to co-intercalate to modify the amount of interlayer water and assess their role on activity. This work provides a platform for studies focused on elucidating the origins of improved intrinsic activity for future confined layered catalyst systems.

Conclusions

In this work we demonstrate an active catalyst motif based on transition metal cations confined within environments of molecular length scales. This motif contains Ni and Fe cations that are bonded to phosphate groups within the water-containing layered structure of zirconium phosphate, producing highly active Fe-rich OER catalysts. We show that modifying the homogeneity of interlayer environment can improve the activity and stability for the OER in a confined space. Improved intrinsic activity is achieved only for mixed metal systems that are fully intercalated. Grafting studies indicate that the activity originates from the species within the interlayer and not those that are surface bound. Computationally, we find that a wycheproofite type structure represents a suitable platform for the octahedral intercalation of cations were bonding occurs via phosphate groups. In this system, by increasing Fe content in M-O-M sites there is a reduction of the OH* to O* potential limiting step (PLS) for Fe-Ni mixtures, due to high-spin Fe^{+3} binding O_{2c} much stronger than low-spin Ni^{+3}. Overall, the enhancement in activity and stability is postulated to originate from the confined environment provided by zirconium phosphate which allows for the synergism with Ni/Fe species and confined water molecules. Future refinement of the catalyst structure along with additional computational analysis and considerations will be necessary to fully understand the role of the interlayer environment. We anticipate that property tuning within confined systems via interlayer engineering is a promising strategy towards further enhancing performance for water oxidation, as well as other reactions of interest.

Experimental Procedures:

Materials

All chemicals were obtained from commercial sources as analytical or reagent grade and used as received. Iron sulfate heptahydrate ($FeSO_4 \cdot 7H_2O$, 99.5%), nickel nitrate hexahydrate ($Ni(NO_3)_2 \cdot 6H_2O$, 98.5%), Nafion 117 (5% solution), zirconyl chloride octahydrate ($ZrOCl_2 \cdot 8H_2O$, 98%), octadecyl isocyanate ($CH_3(CH_2)_{17}NCO$, $\geq$ 90%), and o-xylene ($C_6H_4(CH_3)_2$, analytical standard) were obtained from Sigma-Aldrich (St. Louis, MO). Phosphoric acid (H_3PO_4, 85%) was obtained from Fisher Scientific (Hampton, NH). Glassy carbon rods (SIGRADUR G, HTW Hochtemperatur-Werkstoffe GmbH, 5 mm diameter) were processed by the Stanford University crystal shop to the specifications of a 4 mm height and an area of 0.196 cm^2 where the top side was polished to a surface root-mean-square (rms) roughness of <50 nm. Carbon black was purchased from Fuel Cell Store (College Station, TX, Vulcan XC-72).

Synthesis

θ-Zirconium phosphate: The synthesis of θ-zirconium phosphate was adapted from a literature method.[49] In brief, 100 mL of a 0.05 M solution of $ZrOCl_2 \cdot 8H_2O$ in deionized water was added dropwise (2 ml min^{-1}) to 100 mL of a 0.06 M H_3PO_4 solution that was preheated to 94 °C. This mixture was magnetically stirred for 48 hours at 94 °C. The product was then centrifuged (10,000 RPM for 30 mins) and washed several times (3 times minimum) with deionized water (18.2 MΩ·cm, Merck Millipore, Billerica, MA, USA) and resuspended in a deionized water solution for storage.

α-Zirconium phosphate: θ-zirconium phosphate was converted to α-zirconium phosphate by obtaining a θ-zirconium phosphate gel after centrifuging (10,000 RPM for 30 mins) and subsequently drying it in a vacuum desiccator for > 48 hours. The dried solid was then grounded into a fine powder with a mortar and pestle. Confirmation of successful removal of excess water was confirmed by XRD.

P-0, P-1, P-2, and P-3 Catalyst Synthesis: For P0 catalysts, 30 mg of α-zirconium phosphate in 1 mL of deionized water was used as the precursor material and mixed with 1 mL of a metal salt precursor solution. The metal solution consisted of metal salt precursor ($Fe(NO_3)_2 \cdot 6H_2O$ and/or $Ni(NO_3)_2 \cdot 6H_2O$) at varying metal:α-Zirconium phosphate molar ratios (M:zirconium phosphate). This solution was added to the 1.0 mL suspension of α-zirconium phosphate and left stirring for 48 h. The molar ratios were varied from 10:1 to 1:10 M:zirconium phosphate to produce the various compositions of Ni/Fe modified P0 zirconium phosphate catalysts. For P-1, P-2, and P-3 catalysts, θ-zirconium phosphate was used instead of α-zirconium phosphate.

ODI Modified Zirconium Phosphate: ODI modification of adsorbed and intercalated catalysts followed an adapted procedure from the literature.[58] In short, adsorbed and intercalated zirconium phosphate catalysts were modified by ODI in a three-necked flask. 10 mg of the zirconium phosphate catalyst was dispersed into 25 mL of o-xylene in a three-necked flask and sonically dispersed for 2 hours. ODI was added to the dispersed system at a molar ratio of 10:1 for catalyst to ODI. The mixture was then reacted for 12 hours under nitrogen gas. The mixture was then centrifuged at 10,000 RPM for 30 mins and the product was washed with ethanol several (>3x) times to remove impurities. The ODI modified catalyst was then vacuum dried for 24 hours where the dried solid was then grounded into a fine powder with a mortar and pestle.

Ink Preparation

Modification of the GCD with the catalyst was performed by spin drying a 10 μL drop of the catalyst ink which consisted of the catalyst powder, isopropanol, carbon black, and cation-exchanged Nafion 117 at 600 RPM on the RDE apparatus. The cation-exchanged Nafion 117 was prepared by dissolving 2 mL of Nafion 117 into 1 mL 0.1M KOH. As Nafion is a strong acid, through this process, H^+ is replaced with K^+ to keep the ink condition similar to the electrolyte. Each catalyst ink was prepared by dispersing 5 mg of the catalyst and 1.25 mg of carbon black in 2.55 mL of isopropanol and 10.02 μL of cation-exchanged Nafion 117. The ink was sonicated for >30 minutes or until it was well dispersed. The loading of the working electrode was 100 μg cm^{-2} of catalyst material and 25 μg cm^{-2} of carbon black for a total catalyst loading of 125 μg cm^{-2}. To obtain the amount of Ni/Fe metal content within each catalyst, the wt% was multiplied by 100 μg cm^{-2}.

Electrochemical Measurements

Electrochemical measurements were performed on a VMP-3 potentiostat/galvanostat (BioLogic Science Instruments). Four-point probe measurements were conducted on compressed catalyst powders (15 mg in a 6 mm diameter die at 2000 lbs of applied load) using an in-line four-point probe with 1 mm tip spacing (Lucas Labs, Pro4-4000). Oxygen evolution studies were carried out on a three-electrode electrochemical cell using a rotating disk electrode (RDE) assembly (Pine Research Instrumentation). OER measurements were performed between 0.2 and 1.0 V versus the silver/silver chloride couple (Ag/AgCl) at 10 mV s^{-1} in O_2- saturated 0.1 M KOH electrolyte with an Ag/AgCl reference electrode (Fisherbrand accumet Glass Body Ag/AgCl Reference Electrode – Mercury-Free, Thermo Fischer). The counter electrode was calibrated between each batch of new electrolyte. The counter electrode was a graphite rod and the working electrode was a clean, mirror finish-polished, 5 mm diameter glassy carbon disk (GCD) modified with a zirconium phosphate catalyst. During electrochemical measurements, the working electrode was rotated at 1600 rpm. The rotation speed was fast enough to help in product removal from the surface and limit the bubble formation from oxygen evolution. The solution resistance of the cell was measured at 100 kHz with 20 mV amplitude about the open-circuit potential (OCP), and *i*R-drop compensation occurred after electrochemical testing. The typical solution resistance was 44 – 55 Ω. All potentials were converted and reported herein versus the reversible hydrogen electrode (RHE).

Physical and Chemical Characterization (XRD, ICP-MS, TEM, XAS, and TGA)

X-ray diffraction data were obtained using a D8 VENTURE single-crystal diffractometer (Bruker, λ = 1.5418 Å). The concentration of Fe and Ni of the electrodes and electrolyte was obtained through inductively coupled plasma mass spectrometry (Thermo Scientific, XSERIES 2 ICP-MS). All working electrode samples were digested overnight in an aqua regia matrix before analysis. For electrolyte analysis, aliquots (4 mL) were taken after 0.5, 2, 4, 6, and 8 hr of CA testing fresh electrolyte (0.1 M KOH - 4 mL) was replenished such that the total volume of electrolyte was unchanged. All calibration standards were TraceCERT certified and obtained from Sigma-Aldrich. All XPS spectra were calibrated to the C 1s peak at a binding energy of 284.8 eV. CasaXPS software was used to perform peak fitting with Shirley backgrounds. X-ray absorption spectroscopy was performed at the Stanford Synchrotron Radiation Laboratory (SSRL) in total electron yield mode at beamline 8-2 for the Fe and Ni L-edge. For all experiments, powdered samples were dispersed on carbon tape. For Fe and Ni L-edge spectroscopy, edge-energies were aligned to Ni foil standard sample. All XAS spectra (n=7) were averaged and processed with the Demeter package in Athena. A universal Fe analysis, as described by the literature, was performed on the normalized white line intensities Fe $L_{2,3}$-edges to quantify the amount of ferric iron within zirconium phosphate catalysts.[75] Thermogravimetric experiments (TGA Q500 TA Instruments, New Castle, Delaware, United States) were performed at a ramp rate of 5 °C min^{-1} up to 400 °C under a flow of 100 mL/min of nitrogen gas.

Computational Methods

The density functional calculations were performed within the Vienna ab initio simulation package[80,81] (VASP) using the projector augmented wave (PAW) potentials[82]. We employed the PBE[83] functional together with the Hubbard-U correction method[84] applied for the d-electrons of Ni (U-J=U_{eff} = 6.0 eV) and Fe (U_{eff} = 3.5 eV) atoms[69,85]. The bulk optimization calculations were performed at the energy cutoff of 600 eV on the 4 × 4 × 4 k-point mesh per 2 × 1 × 1 unit cell of the wycheproofite structure. For surfaces, we have employed 2 × 1 symmetric (001) slabs. Here we used 500 eV energy cutoff and the 4 × 4 × k-points. Full relaxation below a minimum threshold force of 0.02 eV/Å^2 was performed in all cases. To obtain the theoretical overpotential for each bulk and surface site, the standard OER mechanism and which has been applied to many types of oxides[65–67,86] ($* \rightarrow OH^*$, $OH^* \rightarrow O^*$, $O^* \rightarrow OOH^*$, $OOH^* \rightarrow O_2(g)$) was assumed. The Gibbs free energies of the OER intermediates calculated via computational hydrogen electrode method[66] include room temperature corrections, zero point energy (ZPE), and the vibrational enthalpy and entropy contributions (relative to $H_2(g)$ and $H_2O(l)$) obtained by means of the harmonic approximation. Combined effect of total energies of adsorption for O2c (O1c) sites were: $\Delta G_{\text{corr.}}$ (OH*)= 0.3343 (0.3393) eV, $\Delta G_{\text{corr.}}$ (O*)= 0.0145 (0.0005) eV, and $\Delta G_{\text{corr.}}$ (OOH*)= 0.3478 (0.3638) eV, respectively. The fully optimized bulk models, reference structures and their respective energies are included as part of the Catalysis-hub.org repository[87].

Acknowledgments:

Fundamental catalyst development was supported by the National Science Foundation Center for Chemical Innovation in Solar Fuels CHE-1305124 and the U.S. Department of Energy, Office of

Science, Office of Basic Energy Sciences, Chemical Sciences, Geosciences, and Biosciences Division, Catalysis Science Program to the SUNCAT Center for Interface Science and Catalysis. The authors would like to acknowledge the use of the computer time allocation for the m2997 allocation at the National Energy Research Scientific Computing Center, a DOE Office of Science User Facility supported by the Office of Science of the U.S. Department of Energy under Contract No. DE-AC02-05CH11231. The authors acknowledge that part of this work was performed at the Stanford Nano Shared Facilities (SNSF), supported by the National Science Foundation under award ECCS-1542152. The authors acknowledge the Stanford University Environmental Measurements Facility and Guangchao Li for ICP-MS measurements. The authors acknowledge the SSRL staff at beamlines 8-2, specifically Dennis Nordlund. Support for J.S. was provided by the Department of Defense (DoD) through the National Defense Science and Engineering Graduate Fellowship (NDSEG) Program and Stanford University Diversifying Academia, Recruiting Excellence Doctoral Fellowship Program (DARE). M.V.R-G. and J.L.C. acknowledge the NSF-PREM Center for Interfacial Electrochemistry of Energy Materials (CIE2M) grant DMR-1827622. M.B.S's work was supported by the Toyota Research Institute.

Author Contributions

J.S. conceived the project, synthesized, characterized, performed electrochemical testing of all catalysts, and drafted the manuscript under the supervision of L.A.K and T.F.J. J.S., M.B.S., and A.G. conducted XAS measurements. A.R.Y. and M.R performed part of the catalyst synthesis and electrochemical assessments. J.S., M.B.S, and L.A.K prepared and revised the original drafts of the manuscript. All authors contributed to data analysis, interpretations, and the final version of the manuscript.

Author ORCID

Joel Sanchez.: 0000-0001-7723-3345

Michaela Burke Stevens: 0000-0003-3584-0600

Alessandro Gallo: 0000-0003-4687-8188

Mario V. Ramos-Garcés: 0000-0002-7511-9941

Jorge L. Colón: 0000-0003-1398-2405
Laurie A. King: 0000-0002-0772-2378
Michal Bajdich: 0000-0003-1168-8616
Thomas F. Jaramillo: 0000-0001-9900-0622

Competing Interests:

The authors declare no competing interests.

Data Availability

All the data needed to support the plots and evaluate the conclusions within this article are present within it, the Supplementary Information, or available from the corresponding author(s) upon request.

Supplementary Information

Supplementary Figs. 1-18, Supplementary Table 1, Supplementary Note 1, and Supplementary References.

References:

1. Suen, N.-T. *et al.* Electrocatalysis for the oxygen evolution reaction: recent development and future perspectives. *Chem. Soc. Rev.* **46**, 337–365 (2017).
2. Wang, H.-F. & Xu, Q. Materials Design for Rechargeable Metal-Air Batteries. *Matter* **1**, 565–595 (2019).
3. Nitopi, S. *et al.* Progress and Perspectives of Electrochemical CO 2 Reduction on Copper in Aqueous Electrolyte. *Chem. Rev.* **119**, 7610–7672 (2019).
4. Song, F. *et al.* Transition Metal Oxides as Electrocatalysts for the Oxygen Evolution Reaction in Alkaline Solutions: An Application-Inspired Renaissance. *J. Am. Chem. Soc.* **140**, 7748–7759 (2018).
5. Burke, M. S., Enman, L. J., Batchellor, A. S., Zou, S. & Boettcher, S. W. Oxygen Evolution Reaction Electrocatalysis on Transition Metal Oxides and (Oxy)hydroxides: Activity Trends and Design Principles. *Chem. Mater.* **27**, 7549–7558 (2015).
6. Lv, L., Yang, Z., Chen, K., Wang, C. & Xiong, Y. 2D Layered Double Hydroxides for Oxygen Evolution Reaction: From Fundamental Design to Application. *Adv. Energy Mater.* **9**, 1803358 (2019).
7. Shi, Q. *et al.* Metal–organic frameworks-based catalysts for electrochemical oxygen evolution. *Mater. Horizons* **6**, 684–702 (2019).

8. Xu, H., Cheng, D., Cao, D. & Zeng, X. C. A universal principle for a rational design of single-atom electrocatalysts. *Nat. Catal.* **1**, 339–348 (2018).

9. Gong, M. & Dai, H. A mini review of NiFe-based materials as highly active oxygen evolution reaction electrocatalysts. *Nano Res.* **8**, 23–39 (2015).

10. Görlin, M. *et al.* Oxygen Evolution Reaction Dynamics, Faradaic Charge Efficiency, and the Active Metal Redox States of Ni–Fe Oxide Water Splitting Electrocatalysts. *J. Am. Chem. Soc.* **138**, 5603–5614 (2016).

11. Batchellor, A. S. & Boettcher, S. W. Pulse-Electrodeposited Ni-Fe (Oxy)hydroxide Oxygen Evolution Electrocatalysts with High Geometric and Intrinsic Activities at Large Mass Loadings. *ACS Catal.* **5**, 6680–6689 (2015).

12. Louie, M. W. & Bell, A. T. An Investigation of Thin-Film Ni–Fe Oxide Catalysts for the Electrochemical Evolution of Oxygen. *J. Am. Chem. Soc.* **135**, 12329–12337 (2013).

13. Trotochaud, L., Young, S. L., Ranney, J. K. & Boettcher, S. W. Nickel–Iron Oxyhydroxide Oxygen-Evolution Electrocatalysts: The Role of Intentional and Incidental Iron Incorporation. *J. Am. Chem. Soc.* **136**, 6744–6753 (2014).

14. Corrigan, D. A. The Catalysis of the Oxygen Evolution Reaction by Iron Impurities in Thin Film Nickel Oxide Electrodes. *J. Electrochem. Soc.* **134**, 377 (1987).

15. Shifa, T. A. & Vomiero, A. Confined Catalysis: Progress and Prospects in Energy Conversion. *Adv. Energy Mater.* **9**, 1902307 (2019).

16. Li, H., Xiao, J., Fu, Q. & Bao, X. Confined catalysis under two-dimensional materials. *Proc. Natl. Acad. Sci.* **114**, 5930–5934 (2017).

17. Remsing, R. C., McKendry, I. G., Strongin, D. R., Klein, M. L. & Zdilla, M. J. Frustrated Solvation Structures Can Enhance Electron Transfer Rates. *J. Phys. Chem. Lett.* **6**, 4804–4808 (2015).

18. Remsing, R. C. & Klein, M. L. Solvation dynamics in water confined within layered manganese dioxide. *Chem. Phys. Lett.* **683**, 478–482 (2017).

19. Hahn, C. & Jaramillo, T. F. Using Microenvironments to Control Reactivity in CO2 Electrocatalysis. *Joule* **4**, 292–294 (2020).

20. Augustyn, V. & Gogotsi, Y. 2D Materials with Nanoconfined Fluids for Electrochemical Energy Storage. *Joule* **1**, 443–452 (2017).

21. Fleischmann, S., Spencer, M. A. & Augustyn, V. Electrochemical Reactivity under Confinement Enabled by Molecularly Pillared 2D and Layered Materials. *Chem. Mater.* acs.chemmater.0c00648 (2020). doi:10.1021/acs.chemmater.0c00648

22. Gauthier, J. A., Dickens, C. F., Chen, L. D., Doyle, A. D. & Nørskov, J. K. Solvation Effects for Oxygen Evolution Reaction Catalysis on IrO 2 (110). *J. Phys. Chem. C* **121**, 11455–11463 (2017).

23. Doyle, A. D., Montoya, J. H. & Vojvodic, A. Improving Oxygen Electrochemistry through Nanoscopic Confinement. *ChemCatChem* **7**, 738–742 (2015).

24. Doyle, A. D., Bajdich, M. & Vojvodic, A. Theoretical Insights to Bulk Activity Towards Oxygen Evolution in Oxyhydroxides. *Catal. Letters* **147**, 1533–1539 (2017).

25. McKendry, I. G. *et al.* Systematic Doping of Cobalt into Layered Manganese Oxide Sheets Substantially Enhances Water Oxidation Catalysis. *Inorg. Chem.* **57**, 557–564 (2018).

26. Thenuwara, A. C. *et al.* Intercalation of Cobalt into the Interlayer of Birnessite Improves Oxygen Evolution Catalysis. *ACS Catal.* **6**, 7739–7743 (2016).

27. Thenuwara, A. C. *et al.* Copper-Intercalated Birnessite as a Water Oxidation Catalyst. *Langmuir* **31**, 12807–12813 (2015).

28. Kang, Q. *et al.* Effect of Interlayer Spacing on the Activity of Layered Manganese Oxide Bilayer Catalysts for the Oxygen Evolution Reaction. *J. Am. Chem. Soc.* **139**, 1863–1870 (2017).

29. Luo, Y. *et al.* Two-Dimensional MoS2 Confined Co(OH)2 Electrocatalysts for Hydrogen Evolution in Alkaline Electrolytes. *ACS Nano* **12**, 4565–4573 (2018).

30. Chen, Z. *et al.* Interface confined hydrogen evolution reaction in zero valent metal nanoparticles-intercalated molybdenum disulfide. *Nat. Commun.* **8**, 14548 (2017).

31. Tang, C. *et al.* Spatially Confined Hybridization of Nanometer-Sized NiFe Hydroxides into Nitrogen-Doped Graphene Frameworks Leading to Superior Oxygen Evolution Reactivity. *Adv. Mater.* **27**, 4516–4522 (2015).

32. Lei, F. *et al.* Metallic tin quantum sheets confined in graphene toward high-efficiency carbon dioxide electroreduction. *Nat. Commun.* **7**, 12697 (2016).

33. Santiago, M. B. *et al.* Layered Inorganic Materials as Redox Agents: Ferrocenium-Intercalated Zirconium Phosphate. *Langmuir* **23**, 7810–7817 (2007).

34. Santiago, M. B. *et al.* NADH Electrooxidation Using Bis(1,10-phenanthroline-5,6-dione)(2,2′-bipyridine)ruthenium(II)-Exchanged Zirconium Phosphate Modified Carbon Paste Electrodes. *Electroanalysis* **18**, 559–572 (2006).

35. Santiago, M. B. *et al.* Effect of Enzyme and Cofactor Immobilization on the Response of Ethanol Oxidation in Zirconium Phosphate Modified Biosensors. *Electroanalysis* **22**, 1097–1105 (2010).

36. Rivera, E. J. *et al.* Vapochromic and vapoluminescent response of materials based on platinum(ii) complexes intercalated into layered zirconium phosphate. *J. Mater. Chem.* **21**, 15899 (2011).

37. Rivera, E. J., Figueroa, C., Colón, J. L., Grove, L. & Connick, W. B. Room-temperature emission from platinum(II) complexes intercalated into zirconium phosphate-layered materials. *Inorg. Chem.* **46**, 8569–8576 (2007).

38. Rivera, E. J. *et al.* Luminescence Rigidochromism and Redox Chemistry of Pyrazolate-Bridged Binuclear Platinum(II) Diimine Complex Intercalated into Zirconium Phosphate Layers. *Inorg. Chem.* **51**, 2777–2784 (2012).

39. Casañas-Montes, B. *et al.* Molybdocene dichloride intercalation into zirconium phosphate nanoparticles. *J. Organomet. Chem.* **791**, 34–40 (2015).

40. González-Villegas, J. *et al.* Poly(ethylene glycol)-modified zirconium phosphate nanoplatelets for improved doxorubicin delivery. *Inorganica Chim. Acta* **468**, 270–279 (2017).

41. Díaz, A. *et al.* Nanoencapsulation of insulin into zirconium phosphate for oral delivery applications. *Biomacromolecules* **11**, 2465–2470 (2010).

42. Díaz, A. *et al.* Direct intercalation of cisplatin into zirconium phosphate nanoplatelets for potential cancer nanotherapy. *Nanoscale* **5**, 11456 (2013).

43. Díaz, A. *et al.* Zirconium phosphate nanoplatelets: a novel platform for drug delivery in cancer therapy. *Chem. Commun.* **48**, 1754 (2012).

44. Sanchez, J., Ramos-Garcés, M. V., Narkeviciute, I., Colón, J. L. & Jaramillo, T. F. Transition Metal-Modified Zirconium Phosphate Electrocatalysts for the Oxygen Evolution Reaction. *Catalysts* **7**, 132 (2017).

45. Ramos-Garcés, M. V. *et al.* Transition Metal-Modified Exfoliated Zirconium Phosphate as an Electrocatalyst for the Oxygen Evolution Reaction. *ACS Appl. Energy Mater.* **2**, 3561–3567 (2019).

46. Ramos-Garcés, M. V. *et al.* Morphology control of metal-modified zirconium phosphate support structures for the oxygen evolution reaction. *Dalt. Trans.* **49**, 3892–3900 (2020).

47. V. Ramos-Garcés, M. *et al.* Water Splitting Electrocatalysis within Layered Inorganic Nanomaterials. in *Water Chemistry* (IntechOpen, 2020). doi:10.5772/intechopen.88116

48. Alberti, G. & Costantino, U. Recent progress in the intercalation chemistry of layered α-zirconium phosphate and its derivatives, and future perspectives for their use in catalysis. *J. Mol. Catal.* **27**, 235–250 (1984).

49. Kijima, T. Direct Preparation of θ-Zirconium Phosphate. *Bull. Chem. Soc. Jpn.* **55**, 3031–3032 (1982).

50. Kolitsch, U. The crystal structure of wycheproofite, NaAlZr(PO4)2(OH)2 H2O. *Eur. J. Mineral.* **15**, 1029–1034 (2004).

51. Rudolf, P. R. & Clearfield, A. X-ray powder structure and Rietveld refinement of the monosodium exchanged monohydrate of .alpha.-zirconium phosphate, Zr(NaPO4)(HPO4).cntdot.H2O. *Inorg. Chem.* **28**, 1706–1710 (1989).

52. Sun, L. *et al.* The effect of guest molecular architecture and host crystallinity upon the mechanism of the intercalation reaction. *J. Colloid Interface Sci.* **333**, 503–509 (2009).

53. Brunet, E., Colón, J. L. & Clearfield, A. *Tailored Organic-Inorganic Materials*. *Tailored Organic-Inorganic Materials* (John Wiley & Sons, Inc, 2015). doi:10.1002/9781118792223

54. Burke, M. S., Kast, M. G., Trotochaud, L., Smith, A. M. & Boettcher, S. W. Cobalt–Iron (Oxy)hydroxide Oxygen Evolution Electrocatalysts: The Role of Structure and Composition on Activity, Stability, and Mechanism. *J. Am. Chem. Soc.* **137**, 3638–3648 (2015).

55. Kibsgaard, J. & Chorkendorff, I. Considerations for the scaling-up of water splitting catalysts. *Nat. Energy* **4**, 430–433 (2019).

56. Han, B. *et al.* Screening Oxide Support Materials for OER Catalysts in Acid. *J. Electrochem. Soc.* **165**, F813–F820 (2018).

57. Yi, Y. *et al.* Electrochemical corrosion of a glassy carbon electrode. *Catal. Today* **295**, 32–40 (2017).

58. Han, L. *et al.* Synthesis and Performance of Functionalized α -Zirconium Phosphate Modified with Octadecyl Isocyanate. *J. Nanomater.* **2018**, 1–9 (2018).

59. Bergerhoff, G. & B. *Crystallographic Databases: Information Content, Software Systems, Scientific Applications*. (International Union of Crystallography, 1987).

60. Belsky, A., Hellenbrandt, M., Karen, V. L. & Luksch, P. New developments in the Inorganic Crystal Structure Database (ICSD): accessibility in support of materials research and design. *Acta Crystallogr. Sect. B Struct. Sci.* **58**, 364–369 (2002).

61. Baker, J. G. *et al.* The Role of Aluminum in Promoting Ni–Fe–OOH Electrocatalysts for the Oxygen Evolution Reaction. *ACS Appl. Energy Mater.* **2**, 3488–3499 (2019).

62. Burns, R. G. *Mineralogical Applications of Crystal Field Theory*. (Cambridge University Press, 1993). doi:10.1017/CBO9780511524899

63. Zhou, Y. & López, N. The Role of Fe Species on NiOOH in Oxygen Evolution Reactions. *ACS Catal.* **10**, 6254–6261 (2020).

64. Liu, Y. *et al.* Electrochemical tuning of olivine-type lithium transition-metal phosphates as efficient water oxidation catalysts. *Energy Environ. Sci.* **8**, 1719–1724 (2015).

65. Friebel, D. *et al.* Identification of Highly Active Fe Sites in (Ni,Fe)OOH for Electrocatalytic Water Splitting. *J. Am. Chem. Soc.* **137**, 1305–1313 (2015).

66. Nørskov, J. K. *et al.* Origin of the Overpotential for Oxygen Reduction at a Fuel-Cell Cathode. *J. Phys. Chem. B* **108**, 17886–17892 (2004).

67. Man, I. C. *et al.* Universality in Oxygen Evolution Electrocatalysis on Oxide Surfaces. *ChemCatChem* **3**, 1159–1165 (2011).

68. Liao, P., Keith, J. A. & Carter, E. A. Water oxidation on pure and doped hematite (0001) surfaces: Prediction of Co and Ni as effective dopants for electrocatalysis. *J. Am. Chem. Soc.* **134**, 13296–13309 (2012).

69. Zaffran, J. *et al.* Influence of Electrolyte Cations on Ni(Fe)OOH Catalyzed Oxygen Evolution Reaction. *Chem. Mater.* **29**, 4761–4767 (2017).

70. Hunter, B. M., Gray, H. B. & Müller, A. M. Earth-Abundant Heterogeneous Water Oxidation Catalysts. *Chem. Rev.* **116**, 14120–14136 (2016).

71. Hunter, B. M. *et al.* Trapping an Iron(VI) Water-Splitting Intermediate in Nonaqueous Media. *Joule* **2**, 747–763 (2018).

72. Li, N. *et al.* Influence of iron doping on tetravalent nickel content in catalytic oxygen evolving films. *Proc. Natl. Acad. Sci.* **114**, 1486–1491 (2017).

73. Enman, L. J. *et al.* Operando X-Ray Absorption Spectroscopy Shows Iron Oxidation Is Concurrent with Oxygen Evolution in Cobalt-Iron (Oxy)hydroxide Electrocatalysts. *Angew. Chemie Int. Ed.* **57**, 12840–12844 (2018).

74. Stevens, M. B., Trang, C. D. M., Enman, L. J., Deng, J. & Boettcher, S. W. Reactive Fe-Sites in Ni/Fe (Oxy)hydroxide Are Responsible for Exceptional Oxygen Electrocatalysis Activity. *J. Am. Chem. Soc.* **139**, 11361–11364 (2017).

75. van Aken, P. A., Liebscher, B. & Styrsa, V. J. Quantitative determination of iron oxidation states in minerals using Fe L 2,3 -edge electron energy-loss near-edge structure spectroscopy. *Phys. Chem. Miner.* **25**, 323–327 (1998).

76. Thenuwara, A. C. *et al.* Nickel Confined in the Interlayer Region of Birnessite: an Active Electrocatalyst for

Water Oxidation. *Angew. Chemie - Int. Ed.* **55**, 10381–10385 (2016).

77. Shan, X. *et al.* Structural water and disordered structure promote aqueous sodium-ion energy storage in sodium-birnessite. *Nat. Commun.* **10**, 1–11 (2019).

78. Amann-Winkel, K. *et al.* X-ray and Neutron Scattering of Water. *Chemical Reviews* **116**, 7570–7589 (2016).

79. Clearfield, A. & Kalnins, J. M. On the mechanism of ion exchange in zirconium phosphates—XIII. *J. Inorg. Nucl. Chem.* **38**, 849–852 (1976).

80. Kresse, G. & Furthmüller, J. Efficiency of ab-initio total energy calculations for metals and semiconductors using a plane-wave basis set. *Comput. Mater. Sci.* **6**, 15–50 (1996).

81. Kresse, G. Ab initio molecular dynamics for liquid metals. *J. Non. Cryst. Solids* **192–193**, 222–229 (1995).

82. Kresse, G. & Joubert, D. From ultrasoft pseudopotentials to the projector augmented-wave method. *Phys. Rev. B* **59**, 1758–1775 (1999).

83. Perdew, J. P., Burke, K. & Ernzerhof, M. Generalized Gradient Approximation Made Simple. *Phys. Rev. Lett.* **77**, 3865–3868 (1996).

84. Dudarev, S. L., Botton, G. A., Savrasov, S. Y., Humphreys, C. J. & Sutton, A. P. Electron-energy-loss spectra and the structural stability of nickel oxide: An LSDA+U study. *Phys. Rev. B* **57**, 1505–1509 (1998).

85. Li, Y.-F. & Selloni, A. Mechanism and Activity of Water Oxidation on Selected Surfaces of Pure and Fe-Doped NiO x. *ACS Catal.* **4**, 1148–1153 (2014).

86. Bajdich, M., García-Mota, M., Vojvodic, A., Nørskov, J. K. & Bell, A. T. Theoretical Investigation of the Activity of Cobalt Oxides for the Electrochemical Oxidation of Water. *J. Am. Chem. Soc.* **135**, 13521–13530 (2013).

87. Winther, K. T. *et al.* Catalysis-Hub.org, an open electronic structure database for surface reactions. *Sci. data* **6**, 75 (2019).